PAPER

Check for updates

Sustainable synthesis of α-alumina nanoparticles: a comparative study of base-mediated crystallization *via* co-precipitation

Fariha Zannat,[a] Md. Ashraful Alam,[a] Pulak Ghosh,[b] Raton Kumar Bishwas ![ORCID] *[a] and Shirin Akter Jahan*[a]

Alpha-alumina (α-Al_2O_3) nanoparticles (NPs) were synthesized *via* a controlled co-precipitation method using three different bases: sodium hydroxide (NaOH), potassium hydroxide (KOH), and ammonium hydroxide (NH_4OH). The influence of each base on the structural, optical, and surface properties of the synthesized nanoparticles was systematically investigated. Characterization techniques, including powder X-ray diffraction (PXRD), dynamic light scattering (DLS), UV-Vis spectroscopy, and zeta potential analysis, were employed. Crystallite sizes, estimated using multiple models, ranged from 54.67 nm to 94.74 nm, with NH_4OH yielding the smallest size and the highest specific surface area (28.36 m^2 g^{-1}). Rietveld refinement confirmed complete α-phase formation for the NaOH- and NH_4OH-derived samples, while the KOH-derived sample exhibited minor potassium oxide impurities. UV-Vis analysis revealed a wide band gap (5.4–5.5 eV), and zeta potential measurements indicated enhanced colloidal stability for samples synthesized using NaOH and NH_4OH. Thermogravimetric and differential scanning calorimetry confirmed α-phase formation between 1047 and 1121 °C. Transmission electron microscopy revealed spherical morphology and nanoscale particle size. These findings highlight the critical role of base selection in tuning the physicochemical properties of α-alumina and demonstrate the effectiveness of NH_4OH in producing fine, phase-pure, and stable α-Al_2O_3 nanoparticles suitable for applications in high-temperature ceramics, electronics, and photocatalysis.

1. Introduction

Alumina (Al_2O_3) is a crucial oxide extensively utilized in ceramics, electrical engineering, and petrochemical sectors.[1,2] Among its polymorphic forms, the alpha phase (α-Al_2O_3), also known as corundum, is particularly valued for its superior thermal stability, high hardness, chemical inertness, and electrical insulating properties.[3–5] These features make α-alumina a critical material in a broad range of industries, including electronics, catalysis, protective coatings, and structural ceramics.[6,7] The α-phase is the most stable crystallographic form of alumina, especially at elevated temperatures, and exhibits a hexagonal close-packed structure.[8,9] Typically, the formation of α-alumina requires calcination at temperatures above 1100 °C, during which metastable transitional phases such as γ-, δ-, or θ-alumina may form and gradually convert to the α-phase.[10]

Therefore, the control of synthesis parameters is essential for obtaining pure α-phase alumina nanoparticles with desirable properties.[11] Among the various synthesis techniques developed to produce alumina nanoparticles, such as sol–gel,[12] hydrothermal,[13] and combustion methods,[14] the co-precipitation approach stands out for its simplicity, scalability, and low production cost.[15,16] This method enables precise control of stoichiometry, particle morphology, and size distribution by adjusting key process parameters.[17] Notably, the nature of the base used during precipitation plays a significant role in influencing the nucleation rate, crystallinity, and final morphology of the product. Different bases introduce varying ionic environments that can affect the hydrolysis and condensation kinetics of the aluminum precursor.[18] Previous studies have typically focused on individual bases, leaving limited comparative insight into how different hydroxides systematically affect crystallite size, morphology, phase stability, and colloidal performance.

This study offers a systematic and comparative evaluation of how different alkaline bases, NaOH, KOH, and NH_4OH, influence the physicochemical characteristics of α-alumina NPs synthesized by co-precipitation. Unlike previous studies

[a] *Institute of Glass and Ceramic Research and Testing (IGCRT), Bangladesh Council of Scientific and Industrial Research (BCSIR), Dhaka-1205, Bangladesh. E-mail: rk_bishwas@bcsir.gov.bd, shirin_akter@bcsir.gov.bd*

[b] *Department of Chemistry, Govt. Tolaram College, Narayanganj, Narayanganj-1400, Bangladesh*

that focused on a single base, this work employs X-ray diffraction along with thermal analysis, optical analysis, morphological observation, and particle size measurements to comprehensively investigate the influence of different bases on the material. The findings offer a practical pathway to tailor nanoparticle properties for advanced ceramic, catalytic, and electronic applications, and highlight ammonium hydroxide as a superior base for producing fine, stable, and phase-pure α-alumina NPs.

2. Materials and methods

2.1. Materials

The chemicals employed in this study included aluminum nitrate nonahydrate [Al(NO₃)₃·9H₂O, 99.60%, Merck, Germany], methanol [99.90%, Merck, Germany], sodium hydroxide, potassium hydroxide, ammonium hydroxide solution (NH₄OH) [25.0%, Merck, Germany] and deionized (DI) water utilized throughout the experimental procedures. The DI water was sourced from the deionized water plant, Inorganic Pigment and Chemical Research Division (IPCRD), IGCRT plant of BCSIR, Bangladesh.

2.2. Synthesis route of alumina

5.0 grams of Al(NO₃)₃·9H₂O were precisely weighed (ATY224, Shimadzu, Japan) and solubilized in 100.0 mL of DI water. The mixture was subjected to continuous stirring (UC 152, Stuart, USA) at ambient temperature for 30.0 minutes to ensure complete solubility of the component. Then the base solution was slowly added to the solution until the pH was precisely adjusted to 9.0, monitored using a pH meter (STARTER 3100, OHAUS, China). The mixture was further stirred for 30.0 minutes, then allowed to stand for 12.0 hours to ensure complete settling of the precipitate. The obtained precipitate was repeatedly washed three times with DI water and three times with ethanol to eliminate ions and any remaining water- and ethanol-soluble impurities. The precipitate was then dried at 110.0 °C for 12.0 hours in an oven (ED115, BINDER, USA) to ensure the complete removal of moisture and volatile organics. Finally, the dried powder was finely crushed using a mortar and then calcined in a muffle furnace (LHTC 08/16, Nabertherm, Germany) at 1200.0 °C for 4.0 hours in air, employing a controlled heating rate of 5.0 °C min⁻¹ to synthesize α-Al₂O₃ powders. The procedure was repeated under identical conditions, with varying the base used for the pH adjustment, namely, (A) sodium hydroxide, (B) potassium hydroxide, and (C) ammonium hydroxide, each at a concentration of 0.01 M.

3. Characterization

3.1. Crystallographic analysis

Powder X-ray diffraction (PXRD) was employed to characterize the crystallinity and crystal structure of the synthesized α-alumina NPs.[19–21] Using X-rays and periodic atom alignments with materials that have a consistent crystalline nanostructure, PXRD is a non-destructive analysis technique. By exposing the powdered sample of α-alumina NPs to an intense single-wavelength X-ray beam, XRD data were collected. Additionally, the crystallographic structure, shape, average size, d-spacing, dislocation density, and lattice parameters were investigated by PXRD. In the SmartLab SE (Rigaku, Japan), the copper cathode tube operating at 50.0 mA and 40.0 kV served as the X-ray power source. Under the standard operation mode (SOM), a one-dimensional scan was performed at a scanning speed of 5° min⁻¹, employing a step size of 0.01° and a standard detector head. The analysis was carried out within a 2θ angular range of 5.0° to 90.0°, employing an incident slit width of 0.5° and a length limiting slit of 10 mm to ensure precise beam definition. The whole powder pattern fitting (WPPF) method, utilized for quantitative analysis with the ICDD PDF5+ standard and crystal symmetry, was explored using VESTA software. The Scherrer equation[22] was employed for crystallite size calculations by PXRD. The Scherrer equation typically yields a smaller crystallite size than the actual value, since it attributes diffraction peak broadening solely to finite crystallite dimensions. In practice, additional contributions from lattice strain, structural defects, and other microstructural factors also broaden the peaks, which leads to an underestimation of the true crystallite size.[23]

$$D = \frac{K\lambda}{\beta \cos\theta} \tag{1}$$

Here, D represents the crystallite size, λ is the wavelength of the X-ray source (Cu tube; $\lambda = 0.1541$ nm), K is the crystallite-shape factor ($k = 0.9$), β is the full width at half maximum, and θ is the diffraction angle or Bragg angle. The interplanar distance between the atoms in a crystal system is expressed as the d-spacing values that were determined employing Bragg's law.[24]

$$d = \frac{n\lambda}{2\sin\theta} \tag{2}$$

Crystallographic analysis of the synthesized NPs included the evaluation of lattice parameters, microstrain, relative intensity, dislocation density, unit cell volume, packing efficiency, preferred growth orientation, specific surface area, and crystallinity index. These parameters were calculated using eqn (3)–(12) as presented below.

Lattice parameter for hexagonal crystal structure,

$$\frac{1}{d^2} = \frac{4}{3}\left\{\frac{h^2 + hk + k^2}{a^2}\right\} + \left(\frac{l^2}{c^2}\right) \tag{3}$$

Micro-strain, $\varepsilon = \dfrac{\beta}{4\tan\theta} \tag{4}$

Dislocation density, $\delta = \dfrac{1}{(D)^2} \tag{5}$

Specific surface area, $S = \dfrac{6 \times 10^3}{\rho \times D} \tag{6}$

Volume of the hexagonal unit cell, $V = a^2c \tag{7}$

$$\text{Crystallinity index, } \mathrm{CI} = \frac{H_{101} + H_{004} + H_{200}}{H_{101}} \quad (8)$$

Relative intensity,

$$\mathrm{RI} = \frac{\text{Intensity of a certain plane,} \ I_c}{\text{Intensity of any three planes,} \ (I_1 + I_2 + I_3)} \quad (9)$$

$$\text{Preference growth, } P = \frac{\mathrm{RI}_{\text{sample}} - \mathrm{RI}_{\text{standard}}}{\mathrm{RI}_{\text{standard}}} \quad (10)$$

$$\text{Atomic packing factor (APF)} = \left(\frac{N_{\mathrm{Al}} V_{\mathrm{Al}} + N_{\mathrm{o}} V_{\mathrm{o}}}{a^2 C} \right) \quad (11)$$

$$\text{Crystallinity (\%)} = \frac{I_{101}}{I_{101} + I_{004} + I_{200}} \times 100 \quad (12)$$

Here H signifies the plane's height, I denotes the plane's peak intensity, "a" and "c" are the lattice parameters of the tetragonal unit cell and hkl correspond to the Miller indices.

3.2. Evaluation of crystallite size through various models

Several techniques, including the Scherrer equation, Williamson–Hall plot, Monshi–Scherrer method, size strain plot model, Shahadat–Scherrer model, and linear straight-line model, were applied to evaluate the crystallite size of the NPs.

3.2.1. Williamson–Hall plot. The Williamson–Hall plot is used to investigate how crystal size and microstrain contribute to broadening of peaks observed in X-ray diffraction patterns.[25]

$$\beta_{\text{total}} \cos \theta = \frac{k\lambda}{D} + 4 \cdot \varepsilon \sin \theta \quad (13)$$

By relating eqn (13) to the typical linear equation ($y = mx + c$), we acquired the crystallite size. By plotting $\beta_{\text{total}} \cos \theta$ on the Y-axis and $4 \sin \theta$ on the X-axis, a straight line is constructed. The intercept provides a means to calculate the crystallite size.

3.2.2. Monshi–Scherrer model. The Monshi–Scherrer model minimizes errors and incorporates all reflections by reformulating the Scherrer equation through logarithmic transformations. According to published research, eqn (14) provides a detailed mathematical expression of this strategy.[26]

$$\ln(\beta) = \ln \frac{1}{\cos \theta} + \ln \frac{k\lambda}{D} \quad (14)$$

Plotting $\ln(\beta)$ versus $\ln(1/\cos \theta)$ as per eqn (14) and aligning with the linear equation ($y = mx + c$), the crystallite size can be assessed from the intercept.

3.2.3. Size-strain plot model. For assessing the strain and crystallite size in anisotropic crystals, the size-strain plot is a commonly used method. By focusing on low angle diffraction peaks with minimal overlap, this method improves the reliability of crystallite size and strain determination. The associated equation for this model is shown as eqn (15) in the referenced study.[27]

$$(d_{hkl} \beta_{hkl} \cos \theta)^2 = \frac{k\lambda}{D} (d_{hkl}^2 \beta_{hkl} \cos \theta) + \frac{\varepsilon_2}{4} \quad (15)$$

By positioning $(d_{hkl} \beta_{hkl} \cos \theta)^2$ on the Y-axis and $(d_{hkl}^2 \beta_{hkl} \cos \theta)$ on the X-axis, eqn (15) was then compared to a straight-line equation to estimate the crystallite size, which was derived from the slope.

3.2.4. Linear straight-line model. The Scherrer equation uses only the widening of a single diffraction peak to determine the crystallite size. For precise materials characterization, comprehensive calculations are therefore essential. The Scherrer equation yields the linear straight model in eqn (16), which is a trustworthy model for evaluating crystallite size.[28]

$$\cos(\theta) = \frac{k\lambda}{D} \times \frac{1}{\beta} \quad (16)$$

Crystallite size was obtained from the intercept of the $1/\beta$ versus $\cos(\theta)$ plot.

3.2.5. Sahadat–Scherrer model. Assuming that strain broadening is separable, this model was established by removing the instrumental broadening contributions from diffraction peak broadening. The Scherrer formula yielded eqn (17), which shows an algebraic expression related to this model. When the straight line crosses the origin, the model's accuracy increases.[29] The Sahadat–Scherrer model's mathematical representation is as follows:

$$\cos(\theta) = \frac{k\lambda}{D_{\text{s–s}}} \times \frac{1}{\text{FWHM}} \quad (17)$$

A linear relationship is obtained by plotting 1/FWHM against $\cos(\theta)$, which results in a straight line. This straight line passes through the origin, following the form of the equation: $y = mx$. The size of crystallites can be calculated by associating $k\lambda/D_{\text{s–s}}$ with the slope of the equation.

3.2.6. Halder–Wagner method. The Halder–Wagner technique states that XRD reflections are not a blend of the Gaussian and Lorentzian profiles, but rather a combination of both. A Lorentzian function describes the tail part, whereas a Gaussian function fits the peak region. This suggests that a Voigt function can correctly represent the XRD pattern. The model evaluates strain using the Gaussian component and determines crystallite size using the Lorentzian component. Eqn (18) provides the mathematical foundation for calculating strain and size using this approach.[30]

$$\left(\frac{\beta_{hkl}}{d_{hkl}} \right)^2 = \left(\frac{1}{D} \right) \left(\frac{\beta_{hkl}}{d_{hkl}^2} \right) + \left(\frac{\varepsilon}{2} \right)^2 \quad (18)$$

Crystallite size can be evaluated from the slope by plotting $\left(\frac{\beta_{hkl}}{d_{hkl}} \right)^2$ along the Y-axis and $\left(\frac{\beta_{hkl}}{d_{hkl}^2} \right)$ along the X-axis using eqn (18). The Halder–Wagner method is based on assumed strain distribution models that are not necessarily applicable to all cases, and its application is comparatively more demanding than simpler approaches, as it requires rigorous analysis and high precision diffraction data.[31]

3.3. Zeta potential and dynamic light scattering

A vial containing 0.1 mg of the generated α-alumina NP powder and 20.0 mL of deionized water was employed as the dispersion

medium. The vial was then placed in an ultrasonic bath for 30.0 minutes to assess the zeta potential (POWER SONIC 510, UK; power: 410 W). DLS was used to measure the change in scattering intensities at a single point caused by the particle's Brownian motion by directing monochromatic light through the sample cell and measuring the autocorrelation function of the photocurrent at a given angle. In this analysis, a zeta potential analyzer and a particle size analyzer (ZSU5700, Malvern Panalytical, UK) were used.

3.4. UV-visible (UV-Vis) spectrophotometry

A UV-1800 spectrophotometer (Shimadzu, Japan) was utilized for UV-Vis analysis in the wavelength range of 200–800 nm and a photometric range of −4 to 4 absorbance and transmittance (0% to 400%). The sample was exposed to UV and near-visible radiation, and radiation absorbance or transmittance was evaluated according to the principles of the Beer–Lambert law.[32] To formulate the sample solution for UV-Vis spectroscopic analysis, 0.2 mg of the synthesized α-alumina NP sample was mixed with 4.0 mL of ethanol solution. The Tauc plot approach,[33] which is based on the following equation, was used to examine the absorption data:

$$(\alpha h\nu)^n = A(h\nu - E_g) \tag{19}$$

In this equation, α stands for the absorption coefficient, $h\nu$ corresponds to the photon energy, E_g is the band gap energy, A is a proportionality constant, and n varies depending on the nature of the electronic transition.

3.5. Thermogravimetric analysis (TGA) and differential scanning calorimetry (DSC)

A Simultaneous Thermal Analyzer (STA) 449 F5 Jupiter (NETZSCH, Germany) was utilized to carry out TGA–DSC analysis. DSC was carried out under a nitrogen atmosphere (for inert conditions) at a heating rate of 5 °C min^{-1}, with a resolution of less than 1 μW, depending on the sensor used. DSC records the changes in enthalpy associated with physical or chemical transformations of α-alumina NPs as a function of time or temperature. TGA was conducted on the same instrument under identical conditions, with a mass resolution of 0.025 μg. TGA monitors the mass loss of α-alumina NPs as the temperature increases, providing insight into various thermal decomposition and transformation processes.

3.6. Transmission electron microscopy (TEM)

The internal morphology and elemental composition of the synthesized α-alumina NPs were examined using a multipurpose TEM integrated with EDS (JEM2100 Plus, JEOL, Japan). The instrument operated at an accelerating voltage of 200 kV to ensure adequate electron beam penetration through the samples. The instrument runs on an input voltage of 210–240 VAC at 50 or 60 Hz, with the maximum loading capacity of 20 A, an input breaker rated at 25 A, and a short-circuit current rating (SCCR) of 10 kA. Elemental analysis was conducted under the same accelerating voltage and a probe current of 7.475 nA using EDS at an accelerating voltage of 200.0 kV, with a real time of

53.06 s, a live time of 50.00 s, an energy range of 0–40 keV, and a probe current of 7.47500 nA. Data were collected using a silicon drift detector (SDD) under PHA (pulse height analysis) mode T3, with a 5% dead time and a counting rate of 4724 counts per s.

4. Results and discussion

4.1. Crystallographic analysis

X-ray diffraction (XRD) is an effective method for evaluating the crystal structure of powdered materials. It reveals key details of the sample, such as crystallinity, phase identity, and purity.[34] Fig. 1 shows the XRD pattern of the synthesized α-alumina NPs. The fabricated NPs were observed to have a hexagonal crystal system within the $R\bar{3}c$ (No. 167) space group, as confirmed by comparison with the ICDD standard [card no. 01-076-8186]. The investigation aimed to examine the structural properties of the materials utilizing various bases for pH regulation. For samples A and C, eight noticeable diffraction peaks were found. In contrast, additional peaks appeared in sample B due to the presence of KOH-related phases. In Fig. 1, the main diffraction angles for sample A observed at 24.810°, 34.389°, 37.011°, 42.594°, 51.7948°, 56.7189°, 65.748°, and 67.418° align with the (012), (104), (110), (113), (024), (116), (214), and (300) miller indices. The heights observed for sample A are 7406 cps, 15 042 cps, 7327 cps, 17 309 cps, 7286 cps, 14 860 cps, and 5119 cps. The prominent diffraction peaks observed for sample B were 25.544°, 34.834°, 36.998°, 43.516°, 51.751°, 56.711°, 65.721°, and 67.412°, while those for sample C were 24.764°, 34.322°, 36.957°, 42.502°, 51.729°, 56.644°, 65.684°, and 67.400°, corresponding to the same Miller indices in both cases. Bishwas et al. reported comparable diffraction peaks associated with the same miller indices.[35] The corresponding peak heights observed for sample B were 485 cps, 437 cps, 4079 cps, 341 cps, 4199 cps, 7501 cps, 2600 cps, and 3834 cps, and those for sample C were 6447 cps, 13 723 cps, 6383 cps, 14 432 cps, 5951 cps, 11 742 cps, 3997 cps, and 6848 cps.

For sample A, the average crystallite size was found to be 68.43 nm for sample A, 94.74 nm for sample B, and 54.67 nm for sample C. Among the three, the smallest crystallite size was exhibited by sample C (Table 1).

The main diffractions for the nanocrystal at 34.799° (104), 42.903° (113), and 56.890° (116) in the ICDD data revealed a slight leftward shift to 34.389°, 42.594°, and 56.719° for sample A, and 34.322°, 42.502°, and 56.644° for sample C. Conversely, a rightward shift was observed for sample B and this contraction is typically associated with a reduced unit cell volume, which shortens the distance between atomic planes. As a result, the Bragg angle increases, causing a rightward shift in the diffraction peaks due to constructive interference at higher 2θ values. The diffraction shifted to 34.834°, 42.502° and 56.644°. A shift toward lower 2θ angles indicates an increase in interplanar spacing, implying lattice expansion within the crystal structure. The expansion is commonly linked to an increase in the unit cell volume, which increases the distance between atomic planes. This greater spacing reduces the Bragg angle, resulting
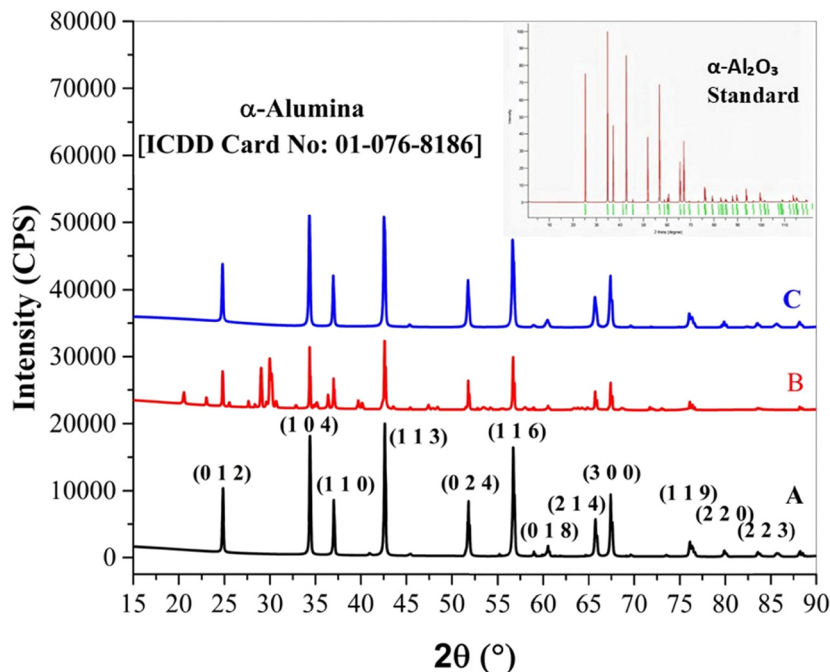
Fig. 1 X-ray diffraction pattern of the prepared α-alumina NPs.

Table 1 Crystallite size calculations for α-alumina NPs

2θ (°)	Reflection	FWHM (°)	Intensity (cps)	Height (cps)	d-Spacing (Å)	Crystallite size, D (nm)	Average crystallite size (nm)
NaOH base (sample A)							
24.810	(012)	0.127	1230	7406	3.5858	66.7	
34.389	(104)	0.125	2544	15 042	2.6058	69.4	
37.011	(110)	0.111	1166	7327	2.42692	78.8	
42.594	(113)	0.123	3078	17 309	2.12085	72.5	68.43
51.7948	(024)	0.125	1149	7286	1.76366	70.0	
56.7189	(116)	0.125	3003	14 860	1.62167	75.1	
65.748	(214)	0.158	1197	5119	1.41913	62.5	
67.418	(300)	0.138	1844	8732	1.38799	72.5	
KOH base (sample B)							
25.544	(012)	0.099	56	485	3.4844	85.5	
34.360	(104)	0.072	842	8617	2.6078	121.1	
36.998	(110)	0.073	548	4079	2.4278	119.7	
42.576	(113)	0.079	1027	9267	2.1217	113.1	94.74
51.751	(024)	0.080	465	4199	1.76503	115.9	
56.711	(116)	0.088	981	7501	1.62189	107.7	
65.721	(214)	0.092	361	2600	1.41965	106.8	
67.412	(300)	0.106	468	3834	1.38810	94.2	
NH$_4$OH base (sample C)							
24.764	(012)	0.131	1203	6447	3.5923	64.9	
34.322	(104)	0.139	2647	13 723	2.6107	62.4	
36.957	(110)	0.131	1175	6383	2.4303	66.7	
42.502	(113)	0.153	3107	14 432	2.12524	58.2	54.67
51.729	(024)	0.183	1525	5951	1.76574	50.5	
56.644	(116)	0.173	2943	11 742	1.62364	54.6	
65.684	(214)	0.218	1152	3997	1.42037	45.3	
67.400	(300)	0.184	1771	6848	1.38831	54.2	

in a leftward shift of the diffraction peaks due to enhanced constructive interference. In contrast, a rightward shift indicates a decrease in interplanar spacing.[36,37]

Tables 2 and 3 present the peak indexing calculations using theta (θ) and inter-planar distance. Three primary diffraction peaks were identified at $2\theta = 34.389°$, $42.594°$ and $56.719°$ for sample A. For sample B, the peaks occurred at 2θ values of $34.834°$, $42.502°$ and $56.644°$, while sample C showed peaks in the (104), (113) and (116) plane, which are completely consistent with the standard data (ICDD Card No. 01-076-8186). The peak profiling information for the synthesized NPs, determined using the diffraction angle (θ), is summarized in Table 2.

Table 2 Profiling of diffraction peaks based on the diffraction angle (θ)

2θ	θ	$1000 \times \sin^2\theta$	Reflection	Remarks
NaOH base (A)				
34.389	17.195	87.3939	(104)	$1^2 + 0^2 + 4^2 = 17$
42.594	21.297	131.9160	(113)	$1^2 + 1^2 + 3^2 = 11$
56.719	28.3595	225.6271	(116)	$1^2 + 1^2 + 6^2 = 38$
KOH base (B)				
34.834	17.417	89.5948	(104)	$1^2 + 0^2 + 4^2 = 17$
42.576	21.288	131.8097	(113)	$1^2 + 1^2 + 3^2 = 11$
56.711	28.355	225.5615	(116)	$1^2 + 1^2 + 6^2 = 38$
NH$_4$OH base (C)				
34.322	17.161	87.0590	(104)	$1^2 + 0^2 + 4^2 = 17$
42.502	21.251	131.373	(113)	$1^2 + 1^2 + 3^2 = 11$
56.644	28.322	225.08	(116)	$1^2 + 1^2 + 6^2 = 38$

Table 3 Diffraction peak profiling by interplanar distance or d-spacing (d)

2θ	θ	d-spacing (Å)	$1000/d^2$	Reflection	Remarks
NaOH base (A)					
34.389	17.195	2.6058	147.2712	(104)	$1^2 + 0^2 + 4^2 = 17$
42.594	21.297	2.1209	222.3207	(113)	$1^2 + 1^2 + 3^2 = 11$
56.719	28.3595	1.6217	380.2551	(116)	$1^2 + 1^2 + 6^2 = 38$
KOH base (B)					
34.834	17.417	2.5735	150.9912	(104)	$1^2 + 0^2 + 4^2 = 17$
42.576	21.288	2.1217	222.1427	(113)	$1^2 + 1^2 + 3^2 = 11$
56.711	28.355	1.6219	380.1519	(116)	$1^2 + 1^2 + 6^2 = 38$
NH$_4$OH base (C)					
34.322	12.650	2.6107	146.7189	(104)	$1^2 + 0^2 + 4^2 = 17$
42.502	19.088	2.1252	221.4033	(113)	$1^2 + 1^2 + 3^2 = 11$
56.644	23.935	1.6236	379.3329	(116)	$1^2 + 1^2 + 6^2 = 38$

The calculated profile values suggest a uniform atomic distribution along specific crystal planes (Miller indices), indicating a preferred crystallographic orientation. Furthermore, the d-spacing-based peak analysis presented in Table 3 supports this observation, confirming preferential growth within the crystal structure of α-alumina NPs.[38,39]

4.1.1. Quantitative analysis by Rietveld refinement in the WPPF method. As shown in Fig. 2, the whole powder pattern fitting (WPPF) technique applies detailed crystal structure and lattice constant information to perform profile fitting across an extensive angular range. This approach enables the concurrent refinement of both diffraction intensity and angle during the pattern fitting process.[40] The experimental XRD data were compared against the reference pattern for α-alumina NPs (ICDD Card No. 01-076-8186). Rietveld refinement using the WPPF method confirmed that samples A, B, and C consisted entirely (100.0%) of the α-alumina phase, exhibiting a hexagonal crystal structure (Table 4).

Fig. 2 illustrates the synthesis of 100% α-alumina NPs for samples A and C and 97.1% α-alumina NPs with 2.9% potassium oxide for sample B under varying fitting conditions (R_{wp} = 46.34%, R_p = 31.43%, S = 1.8121, χ^2 = 3.2836 for sample A; R_{wp} = 41.26%, R_p = 29.29%, S = 1.5154, χ^2 = 2.2963 for sample B; and R_{wp} = 44.46%, R_p = 31.32%, S = 1.7806, χ^2 = 3.1705 for sample C). Crystal lattice parameters were obtained through structural refinement using the Rietveld approach. The refined lattice parameters for the nanoparticles were determined to be $a = b = 4.8267$ Å, $c = 13.1019$ Å (sample A), $a = b = 4.8002$ Å, $c = 13.117$ Å (sample B), and $a = b = 4.8324$ Å, $c = 13.187$ Å (sample C), all with $\alpha = \beta = 90.0°$, $\gamma = 120.0°$. In contrast, the corresponding standard values were $a = b = 4.807$ Å, $c = 13.116$ Å; $\alpha = \beta = 90.0°$ $\gamma = 120$ (Table 5).

4.1.2. Crystallite size estimation employing multiple models. Several analytical models, such as the Williamson–Hall plot, Monshi–Scherrer method, size-strain plot model, linear-straight-line model, Sahadat–Scherrer model and Halder–Wagner method (refer to eqn (13)–(18)), were applied to determine the crystallite size of the synthesized α-alumina NP samples A, B and C. Their crystallite sizes are summarized in Table 6.

The Williamson–Hall plot extends the Scherrer equation by incorporating the impact of microstrain within the crystal lattice, which also contributes to peak broadening. It is assumed that the overall broadening of X-ray diffraction peaks results from a combination of size-induced broadening and strain effects, which are caused by the limited crystallite size, and strain broadening, which is caused by lattice distortions, or microstrain, in the material, which forms the basis of the Williamson–Hall plot.

Through the analysis of several diffraction peaks, the Monshi–Scherrer model enhances crystallite size determination by enabling precise average size and taking crystal anisotropy into account. The Scherrer equation was modified to minimize mistakes and incorporate all reflections for determining crystallite size by rearranging it and applying the logarithm to both sides. For nanoscale materials with high strain, this minimizes the inaccuracies common in conventional Scherrer calculations. Averaging several diffraction peaks along with partial correction for anisotropic broadening leads to an increased calculated crystallite size that was achieved using this model as opposed to the conventional Scherrer equation. The model's multi-peak structure tends to lessen the underestimation seen in single-peak approaches, offering a more precise estimate for nanomaterials with moderate strain even though it does not specifically account for microstrain.

The size strain plot model analyzes strain effects and crystallite size in a single computation by using a linear plot. This yields a more accurate approximation than approaches that presume that strain or size alone is the cause of broadening. The SSP model is appropriate for materials having anisotropic (direction-dependent) characteristics since it takes several crystal planes into consideration. By considering multiple peaks, the errors arising from dependence on just one diffraction peak can be reduced. The SSP model reduces these assumptions, enabling a more precise assessment of crystallite size and strain, in contrast to the Scherrer model, which assumes that peak broadening is mostly caused by crystallite size. This is particularly helpful for materials at the nanoscale, where peak broadening is greatly influenced by both factors.

The linear straight-line model, a variant of the Scherrer model, is widely used to estimate crystallite size. In contrast to the other models, this approach predicted a noticeably bigger crystallite size, suggesting that this material system is not very reliable. The primary limitation arises from the model's assumption of negligible strain and instrumental
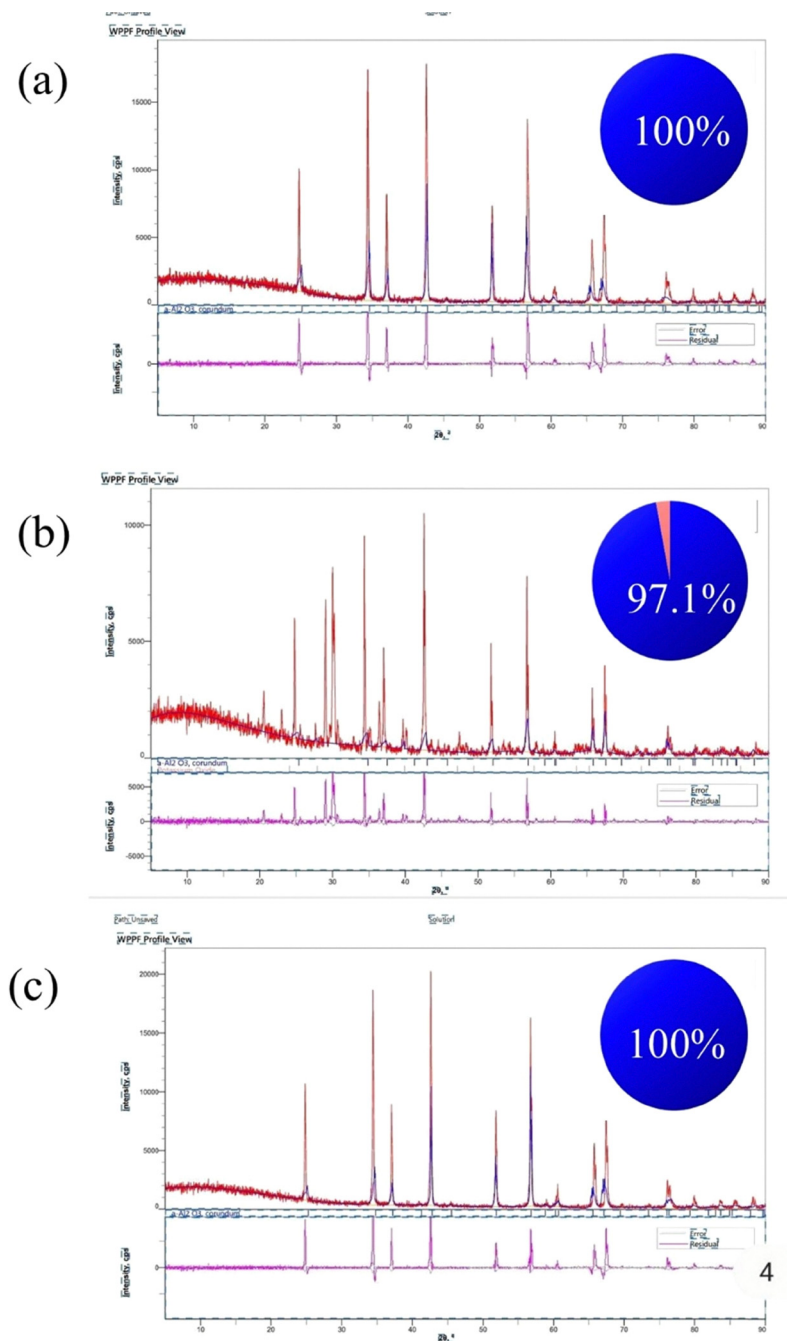
Fig. 2 Quantitative analysis of α-alumina NPs by the WPPF method.

broadening effects, which causes systems, where peak broadening is not exclusively attributable to crystallite dimensions, to overestimate size. The model's applicability for α-alumina is further diminished by the significant deviation in linear fitting introduced by the substantial variety in peak widths across various reflections.

The Sahadat–Scherrer model calculates crystal size more accurately, overcoming the drawbacks of the linear straight-line model. There are multiple crystallite size restrictions (crystallite size with a larger value) in the models discussed above. Thus, it is essential to overcome these restrictions. That is why the

Sahadat–Scherrer model is illustrated. One benefit of this model is that it provides a more accurate crystal size since it accounts for the straight line that passes through the origin. The estimated crystallite sizes are in good agreement with the results calculated using the traditional Scherrer equation, demonstrating that this approach effectively minimizes overestimation without compromising analytical ease.

According to the Halder–Wagner technique, the XRD reflection is a combination of both a Lorentzian and a Gaussian function. This approach states that a Lorentzian function governs the reflection's tail. According to the Halder–Wagner

Table 4 Estimated crystallographic parameters of the synthesized α-alumina NPs

Parameters	Sample A	Sample B	Sample C
Average crystallite size (nm)	68.43	94.74	54.67
Microstrain	0.000250	0.000179	0.00327
Lattice parameters	$a = b = 4.8267$ Å, $c = 13.102$ Å	$a = b = 4.8002$ Å, $c = 13.117$ Å	$a = b = 4.8324$ Å, $c = 13.178$ Å
Angular parameters	$\alpha = \beta = 90°$, $\gamma = 120°$	$\alpha = \beta = 90°$, $\gamma = 120°$	$\alpha = \beta = 90°$, $\gamma = 120°$
Crystallinity (%)	35.69	36.02	35.73
Lattice volume (Å³)	264.344	261.738	266.516
Crystal strain (%)	0.150	0.153	0.174
Dislocation density (nm^{-2})	0.000217	0.000120	0.000351
Specific surface area (m² g^{-1})	22.66	16.36	28.36
Crystallinity index	2.727	2.104	2.764
Preference growth	0.132	0.544	0.114

method, an XRD peak is a mix of two shapes, Lorentzian and Gaussian. The Lorentzian part represents the tail of the peak, while the Gaussian part describes its main body. Together, they form a Voigt function. In this method, the crystallite size is calculated using the Lorentzian part, and the strain is estimated using the Gaussian part. The Halder–Wagner equation is then used to determine both size and strain.

Among the models applied, the size-strain plot and Halder–Wagner models demonstrated the best correlation, as evidenced by their highest R^2 values during analysis.

4.1.3. Structural mechanism. The structures illustrated in Fig. 3 were created with the aid of VESTA software, based on structural parameters for Al_2O_3 NPs, with the Al atom located at $x = 0.000$, $y = 0.333$ and $z = 0.000$ and the O atom at $x = 0.166$, $y = 0.166$ and $z = 0.220$. α-Alumina (Al_2O_3) exhibits a hexagonal crystal structure and belongs to the rhombohedral space group $R\bar{3}c$ (space group no. 167). The structural visualization using VESTA software provided a clear representation of the crystal framework of α-alumina NPs. Ball-and-stick and plane model visualizations reinforced the identification of dominant atomic arrangements and confirmed uniformity across samples in terms of crystallographic symmetry and atomic coordination. Fig. 3 shows the crystal structure dominant plane of α-alumina NPs, where Fig. 3(a–c) depict the ball-and-stick representations for samples A, B, and C, respectively, while Fig. 3(d–f) illustrate the corresponding predominant planes.

A strong diffraction peak observed along the (113) plane indicates a preferred orientation and significant atomic alignment in this direction.[41] The angular parameters remain consistent across all samples, with $\alpha = \beta = 90.00°$ and $\gamma = 120.00°$. The lattice parameters for the samples are as follows: sample A exhibits $a = b = 4.8267$ Å and $c = 13.1019$ Å; sample B shows $a = b = 4.8002$ Å and $c = 13.117$ Å; and sample C has $a = b = 4.8324$ Å and $c = 13.178$ Å. For all three samples, the highest intensity diffraction peak is observed along the (113) plane, indicating a preferred crystallographic orientation and suggesting a higher degree of atomic alignment in this direction.

4.2. Band gap analysis

The optical band gap of α-alumina NPs was evaluated using the Tauc plot method (eqn (19)), as shown in Fig. 4, where $(\alpha h\nu)^n$ was plotted against $h\nu$. The band gap energy was determined by extrapolating the linear segment of the curve to the photon energy axis. The extrapolation yielded the calculated band gap of the synthesized NPs. The best linear fit was obtained for $n = 2$, confirming an allowed indirect transition.[42] This value aligns with the characteristic band gap range of the α-alumina phase, typically reported between 5.0 and 6.0 eV.[43] The slight differences in band gap values may be attributed to variations in crystallite size, lattice strain, and surface defects introduced during synthesis. The synthesized NPs exhibit a wide band gap of about 5.4–5.5 eV, indicating strong insulating behavior. Its excellent thermal conductivity and chemical inertness further support its integration in electronic, optical, and high-temperature technologies.[44] These combined properties make it highly desirable for advanced functional applications. A material with a higher band gap energy typically has stronger atomic bonds, which increases the material's mechanical strength. Wide band gaps in nanoparticles are usually associated with higher hardness and thermal stability. Among the synthesized samples, sample C exhibited the highest band gap energy (5.58 eV), followed by sample A (5.53 eV) and sample B (5.54 eV).

4.3. Hydrodynamic diameter and zeta potential analysis

Fig. 5 presents the size distribution scatter pattern acquired through DLS analysis, with Fig. 5(a–c) showing the DLS size distribution results for samples A, B, and C, respectively. Dynamic light scattering (DLS) was conducted to evaluate the hydrodynamic diameter of the prepared α-alumina NPs.[45–47] The hydrodynamic diameters were 492.3 nm for sample A, 420.0 nm for sample B, and 418.12 nm for sample C, indicating relatively comparable size distributions among the samples. The nanoparticles synthesized using the NH_4OH base (sample C) showed a polydispersity index (PDI) of 0.4341, reflecting slight agglomeration, yet the majority of particles were predominantly within the nanoscale domain. Nanoparticles synthesized using the NaOH base (sample A, PDI = 0.516) and the KOH base (sample B, PDI = 0.6124) exhibited higher polydispersity, reflecting increased heterogeneity in particle size. This reflects greater agglomeration and less controlled growth compared to those produced using NH_4OH as the base.

Sample C demonstrated the smallest hydrodynamic diameter among all samples, indicating better dispersion and lower agglomeration compared to samples A and B.

Fig. 6 presents the zeta potential measurements obtained by electrophoretic light scattering (ELS), where Fig. 6(a–c)

Table 5 Comparison study and quantitative analysis of the synthesized α-alumina NPs

Comparison study of experimental (Exp.) and standard (Std.) diffraction data for sample A

2θ (Exp.)	2θ (Std.)	d (Å) (Exp.)	d (Å) (Std.)	Intensity, I (cps) (Exp.)	Intensity, I (cps) (Std.)	Crystallinity (%) (Exp.)	Crystallinity (%) (Std.)
34.389	34.799	2.6058	2.57591	82.66	100.0	35.69	33.92
42.594	42.904	2.1209	2.10621	100.00	98.6		
56.719	56.890	1.6217	1.61717	97.56	96.2		

Quantitively analysis by the WPPF method

Pattern fitting conditions	Lattice volume (Å³)	Strain (%)	Phase (%)	Lattice parameters
	264.344	0.15	100 [corundum]	$a = b = 4.8267$ Å, $c = 13.1019$ Å; $\alpha = \beta = 90.0°$, $\gamma = 120.0°$

R_{wp}, 46.34%; R_p, 31.43%; S, 1.8121; χ^2, 3.2836
Lattice parameters [corundum: 01-076-8186] [Std.] $a = b = 4.807$ Å, $c = 13.116$ Å; $\alpha = \beta = 90.0°$, $\gamma = 120.0°$; volume: 262.47 Å³; MolVol: 34.01; calculated density: 3.87 g cm⁻³; structural density: 3.87 g cm⁻³; space group: $R\bar{3}c$ (167)

Comparison study of experimental (Exp.) and standard (Std.) diffraction data for sample B

2θ (Exp.)	2θ (Std.)	d (Å) (Exp.)	d (Å) (Std.)	Intensity, I (cps) (Exp.)	Intensity, I (cps) (Std.)	Crystallinity (%) (Exp.)	Crystallinity (%) (Std.)
34.834	34.799	2.5735	2.5759	82.03	100.0	36.02	33.92
42.576	42.904	2.1217	2.1062	100.00	98.6		
56.711	56.890	1.6219	1.6172	95.58	96.2		

Pattern fitting conditions

Pattern fitting conditions	Lattice volume (Å³)	Strain (%)	Phase (%)	Lattice parameters
	261.738	0.1526%	97.1 [corundum]	$a = b = 4.8002$ Å, $c = 13.117$ Å; $\alpha = \beta = 90.0°$, $\gamma = 120.0°$

R_{wp}, 41.26%; R_p, 29.29%; S, 1.5154; χ^2, 2.2963

Comparison study of experimental (Exp.) and standard (Std.) diffraction data for sample C

2θ (Exp.)	2θ (Std.)	d (Å) (Exp.)	d (Å) (Std.)	Intensity, I (cps) (Exp.)	Intensity, I (cps) (Std.)	Crystallinity (%) (Exp.)	Crystallinity (%) (Std.)
34.322	34.799	2.6107	2.57591	85.19	100.0	35.73	33.92
42.502	42.904	2.1252	2.10621	100.00	98.6		
56.644	56.890	1.6236	1.61717	94.72	92.2		

Quantitively analysis by the WPPF method

Pattern fitting conditions	Lattice volume (Å³)	Strain (%)	Phase (%)	Lattice parameters
	266.516	0.174	100 [corundum]	$a = b = 4.8324$ Å, $c = 13.178$ Å; $\alpha = \beta = 90.0°$, $\gamma = 120.0°$

R_{wp}, 44.46%; R_p, 31.32%; S, 1.7806; χ^2, 3.1705

Table 6 Calculated crystallite sizes of the synthesized α-alumina using various models

Method	Crystallite size (nm) for sample A	Correlation coefficient (R^2)	Crystallite size (nm) for sample B	Correlation coefficient (R^2)	Crystallite size (nm) for sample C	Correlation coefficient (R^2)
Williamson–Hall plot	69.69	−0.1558	73.38	0.06148	85.08	−0.1558
Monshi–Scherrer method	70.04	0.437	84.49	−0.166	64.92	0.8151
Linear-straight-line model	249.06	−0.1663	307.17	0.01759	167.27	0.1951
Sahadat–Scherrer model	75.37	0.9796	105.87	0.9523	61.09	0.9780
Size-strain plot	63.04	0.9959	74.56	0.9732	67.98	0.9757
Halder–Wagner method	96.47	0.994	81.54	0.968	89.99	0.981
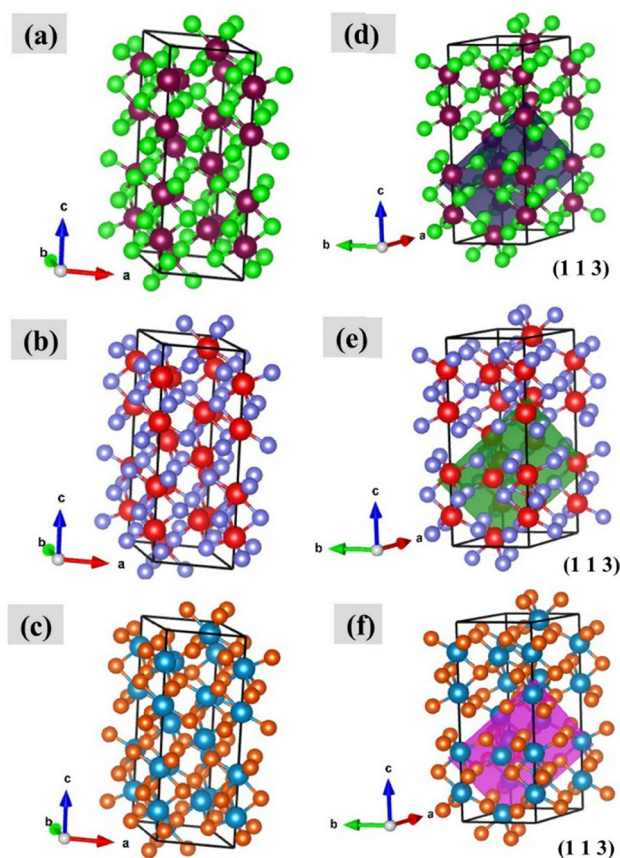
Fig. 3 Crystal structure of the synthesized α-alumina NPs: (a) sample A, (b) sample B, and (c) sample C, and (d)–(f) their corresponding (113) crystal planes.

correspond to samples A, B, and C, respectively. In general, any particles that have a zeta potential higher than ±30 mV are typically electrostatically stable.[48]

Sample A demonstrated a zeta potential range from −28.65 mV to 33.86 mV, whereas sample B exhibited a narrower range of −31.62 mV to +4.75 mV, and sample C showed a range from −22.36 mV to +34.01 mV. Zeta potential measurements revealed that samples prepared using NaOH and NH₄OH bases exhibited broader potential ranges, indicating superior colloidal stability.

DLS analysis indicated that sample C possessed the smallest hydrodynamic diameter, reflecting better particle dispersion and reduced agglomeration, whereas sample A exhibited the largest size. ELS results showed that samples A and C had wider

zeta potential ranges, suggesting improved colloidal stability relative to sample B. These findings highlight the significant role of the base in controlling both hydrodynamic diameter and surface charge, with NH₄OH promoting finely dispersed particles and both NaOH and NH₄OH bases enhancing electrostatic stabilization.

These samples maintained particle dispersibility due to higher surface charges, which is advantageous for applications involving suspensions or coatings. In contrast, the KOH-based sample showed a narrower potential range, implying reduced electrostatic repulsion and lower stability.

4.4. Thermogravimetric and differential scanning calorimetry analyses

TGA–DSC curves of the synthesized NPs (Fig. 7–9) reveal multiple stage mass loss behavior associated with the stepwise dihydroxylation of Al(OH)₃ to Al₂O₃. As can be seen from the TGA curve, in sample A, the mass loss began at approximately 89.19 °C and was completed around 1140.24 °C, resulting in a total reduction of 38.96%. Distinct stages were identified: 17.57% (86.84–254.62 °C), 10.14% (255.12–445.63 °C), 4.64% (446.21–725.35 °C), and 5.67% (726.57–1123.80 °C). The cumulative mass loss corresponds to the release of volatile decomposition products, confirming that thermal decomposition proceeds through the elimination of water components and ultimately yields aluminum oxide as the sole product. The substantial residual mass of 61.04% up to 1200 °C reflects better thermodynamic resistance during subsequent high temperature processing. In the case of sample B, decomposition started at 86.39 °C and finished near 1091.37 °C, with a cumulative loss of 65.27%. Sequential reductions were 25.45% (86.39–209.6 °C), 15.17% (210.29–286.45 °C), 13.90% (287.82–619.10 °C), 6.85% (620.13–788.94 °C), and 5.47% (789.59–1091.37 °C). The higher overall mass loss compared with sample A is attributed to water evolution and volatile impurities, including potassium oxide species. The residual mass at 1200 °C was 34.73%. For sample C, thermal decomposition started at 81.70 °C and ended by 1033.86 °C, resulting in a total weight loss of 55.72%. Individual stages comprised 25.71% (81.70–260.92 °C, 13.64% (261.61–460.98 °C), 13.84% (461.04–912.41 °C), and 2.54% (913.53–1033.28 °C). A final mass of 44.28% remained at 1200 °C, indicating moderate thermal resilience.

The thermal phase transitions of Al(OH)₃ were investigated by differential scanning calorimetry (DSC) over the temperature range of 30 °C to 1200 °C. Fig. 7–9 present the DSC curves of
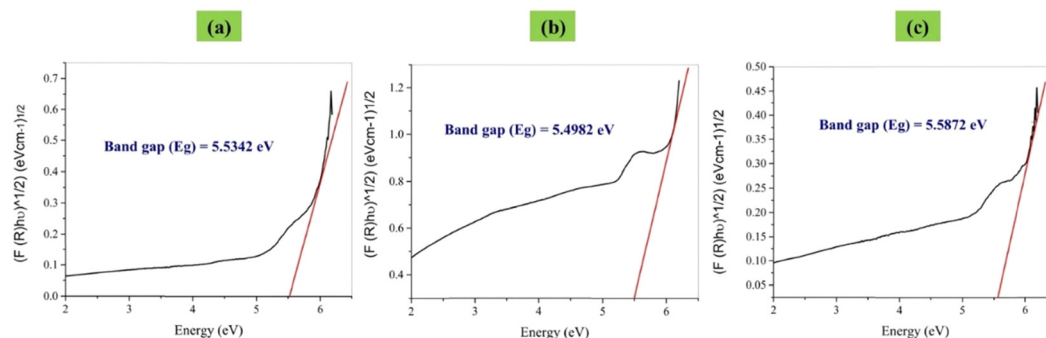
Fig. 4 Tauc's curve for the band gap of (a) sample A, (b) sample B and (c) sample C.
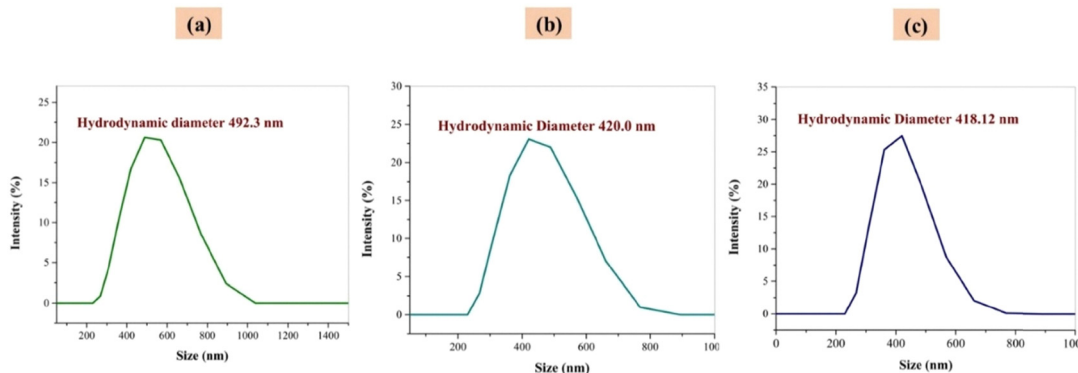

Fig. 5 Particle size distribution curves for (a) sample A, (b) sample B, and (c) sample C.
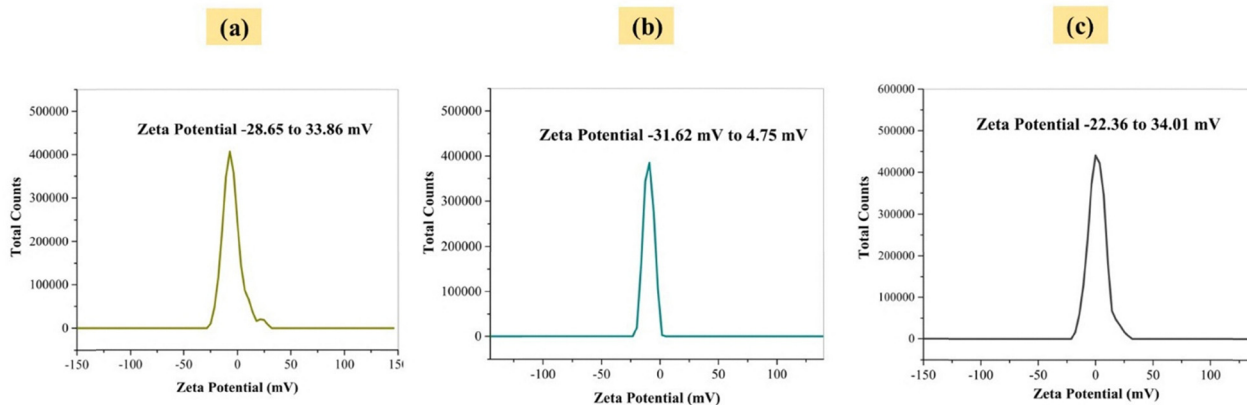

Fig. 6 Zeta potential distribution curves for (a) sample A, (b) sample B, and (c) sample C.

samples A, B, and C. For sample A, an endothermic feature extending from about 51.87 °C to 112.41 °C is associated with the release of physically bound water.[49] The DSC curve displays an endothermic peak at 885 °C, which is attributed to the γ-Al_2O_3 to δ-Al_2O_3 phase transition. A subsequent exothermic event near 1121.4 °C signifies the formation of the α-Al_2O_3 phase.[50] For sample B, the DSC curve shows a broad endothermic feature from about 54.22 °C to 103.28 °C, attributed to

the release of physically absorbed water. An endothermic peak at 446.4 °C followed by an exothermic peak at 582.0 °C is associated with the presence of impurities. An exothermic peak at approximately 1075.1 °C indicates the onset of α-Al_2O_3 crystallization. In the case of sample C, the DSC profile shows a broad endothermic feature between 51.87 °C and 100.93 °C, corresponding to the removal of physically bound water. An endothermic peak at 873.9 °C is attributed to the γ-Al_2O_3
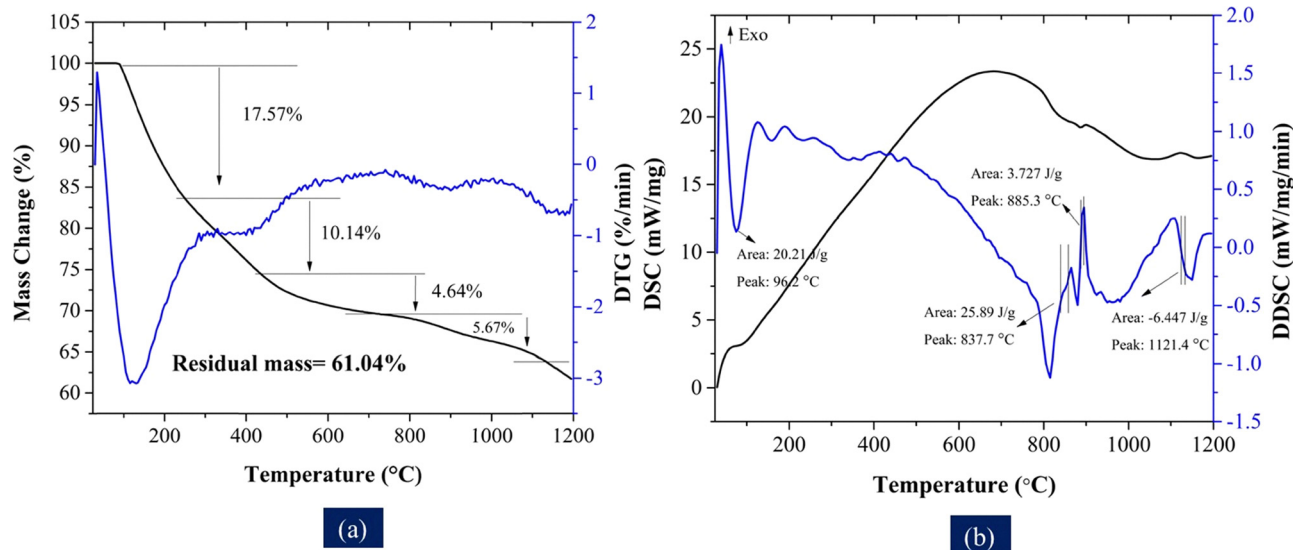
Fig. 7 (a) Thermogravimetric and (b) differential scanning calorimetry analyses of sample A.

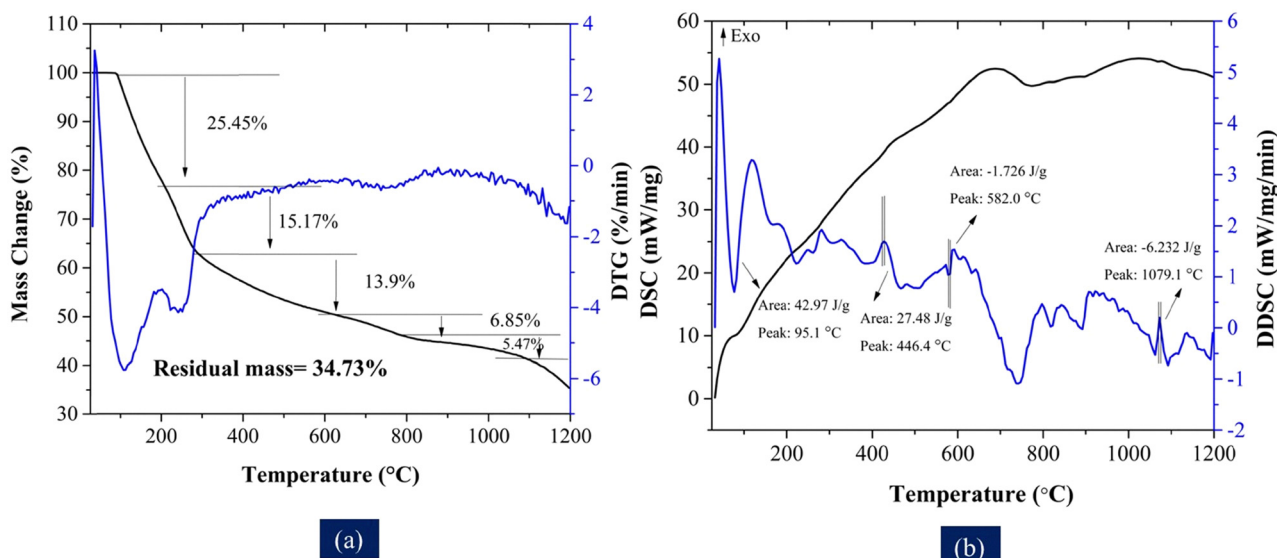Fig. 8 (a) Thermogravimetric and (b) differential scanning calorimetry analyses of sample B.

to δ-Al_2O_3 phase transition. Formation of α-Al_2O_3 is indicated by the exothermic peaks observed at 1047.5 °C and 1121.4 °C. In the comparison of TGA–DSC curves among the three samples, sample A showed the lowest mass loss (38.96%) and the highest residual mass (61.04%), indicating its superior thermal stability, while sample B had the highest mass loss (65.27%) due to volatile impurities. Sample C exhibited intermediate behavior (55.72% mass loss). DSC analysis revealed slight differences in the γ-Al_2O_3 to δ-Al_2O_3 transition temperatures, whereas α-Al_2O_3 formation occurred between 1047 and 1121 °C.

4.5. Transmission electron microscopy analysis

4.5.1. Internal morphology analysis. TEM analysis was carried out to examine the internal morphology of the synthesized

α-alumina nanoparticles.[51] As shown in Fig. 10a–c, the particles predominantly displayed faceted hexagonal domains, consistent with the crystallographic structure of α-alumina. Some regions exhibited partial fusion, which we attribute to agglomeration during calcination. To obtain reliable particle size distributions, measurements were performed on well-dispersed regions of the micrographs, and more than 150 particles were analyzed using ImageJ. The histograms (Fig. 10d–f) follow a Gaussian distribution, yielding average particle sizes of 71.34 nm for sample A, 95.78 nm for sample B, and 57.48 nm for sample C, confirming their nanoscale dimensions. Notably, particle sizes observed by TEM were larger than the crystallite sizes estimated from XRD, indicating that individual TEM-observed particles consist of multiple crystallites.
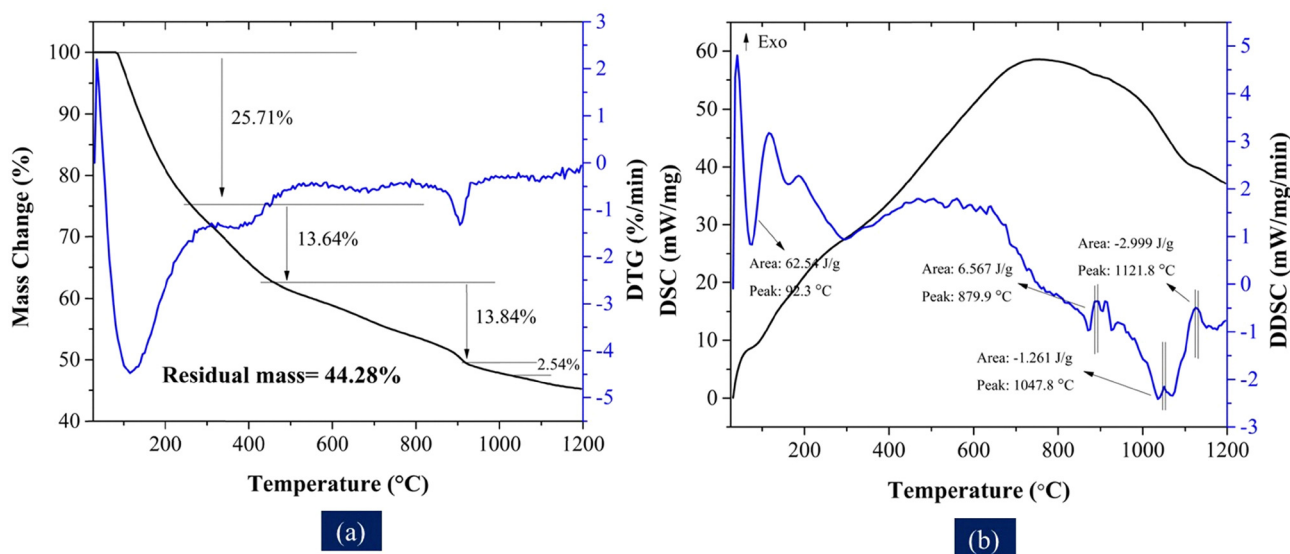
Fig. 9 (a) Thermogravimetric and (b) differential scanning calorimetry analyses of sample C.
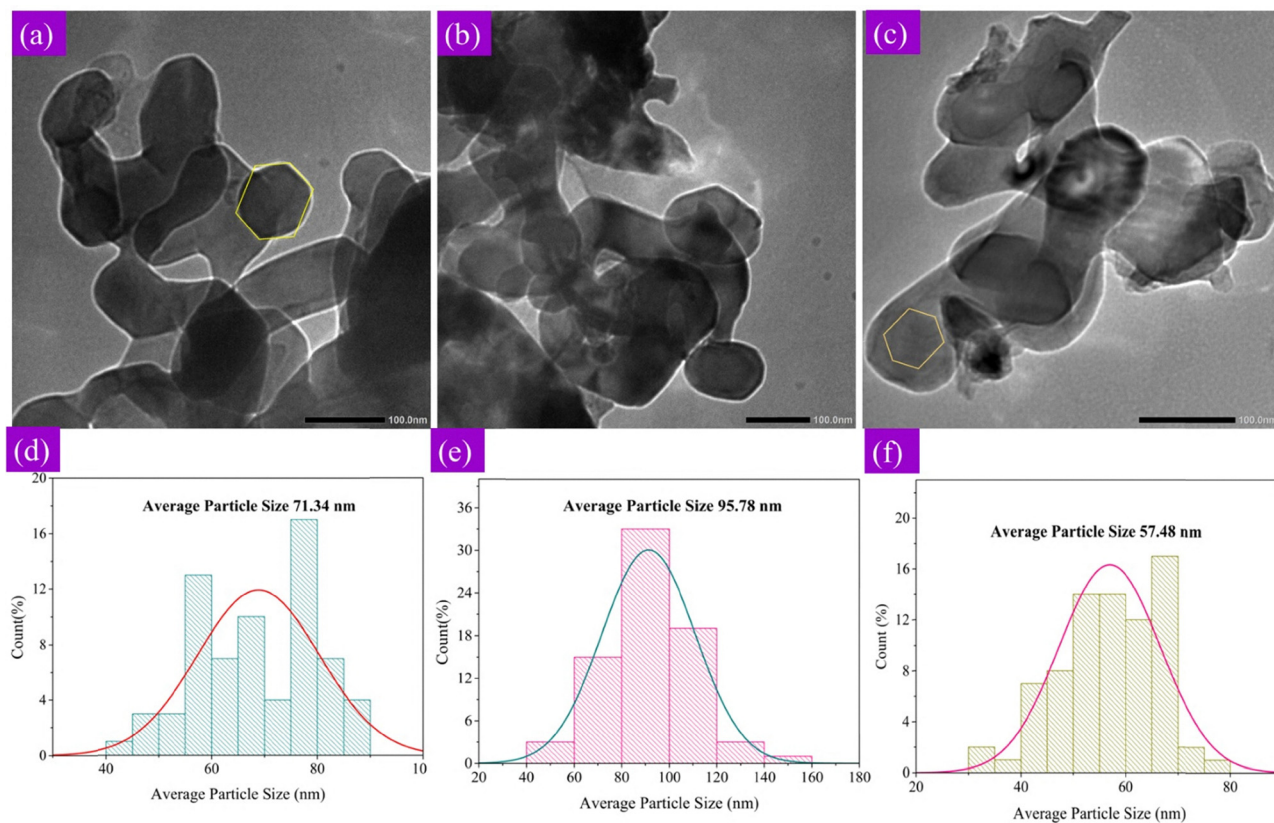

Fig. 10 Internal morphology analysis of α-alumina NPs.

The variation in particle size across samples reflects the influence of base selection during synthesis. Sample B, prepared using KOH, exhibited greater agglomeration and the largest average particle size, likely due to reduced nucleation efficiency and clustering effects. In contrast, sample A (NaOH) and sample C (NH$_4$OH) showed relatively uniform particle distributions and smaller average sizes, with the NH$_4$OH-derived sample exhibiting the lowest clustering degree. This interpretation is supported by its lower polydispersity index (PDI = 0.321) compared to the NaOH- and KOH-derived

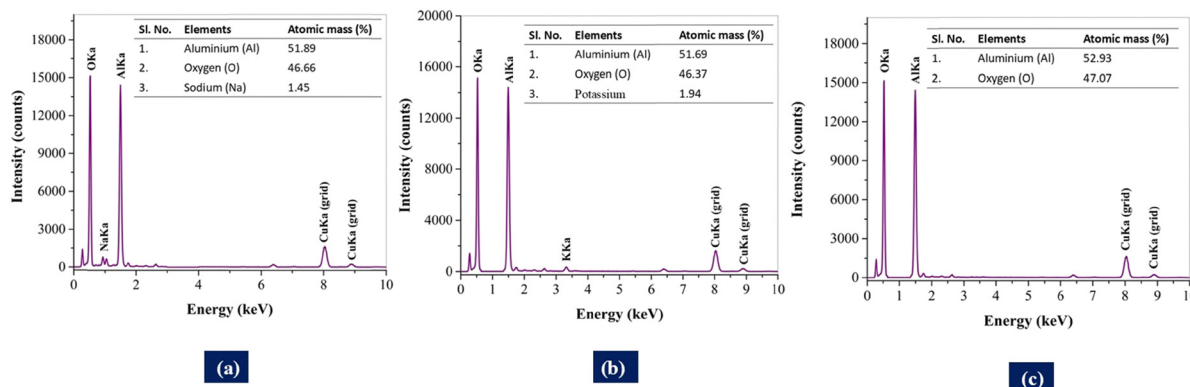**Fig. 11** EDS pattern of the synthesized α-alumina NPs.

samples, indicating enhanced dispersion and surface reactivity. The particle size range obtained here aligns well with values reported in the literature,[52] further validating our findings.

4.5.2. Energy dispersive spectroscopy (EDS) analysis. Energy dispersive spectroscopy (EDS) facilitates microscale elemental analysis, allowing the identification of constituent elements and the detection of possible impurities within the sample.[53] Fig. 11 presents the elemental profile of the synthesized α-alumina NPs through EDS analysis. Distinct peaks corresponding to aluminium, oxygen, and sodium were detected in sample A; aluminium, oxygen, and potassium in sample B; and only aluminium and oxygen in sample C, thereby confirming their respective elemental compositions. Additional signals of carbon and copper were observed, which originated from the carbon coated copper grid used to ensure electrical conductivity during the analysis.

The EDS results for sample C revealed atomic mass percentages of aluminium (52.93%) and oxygen (47.07%), with no detectable impurities. The lack of additional elemental signals beyond aluminium and oxygen confirms the high purity of the synthesized α-alumina NPs. Sample A was composed of aluminium (51.89%), oxygen (46.66%), and sodium (1.45%), while in sample B, aluminium (51.69%), oxygen (46.37%), and potassium (1.94%) were identified. The synthesized α-alumina NPs exhibit complete purity, confirming their uniformity and phase purity in the sample.

5. Conclusion

This study demonstrates the significant influence of base selection on the synthesis of α-alumina NPs *via* co-precipitation. Using aluminum nitrate as the precursor, three bases, NaOH, KOH, and NH_4OH, were evaluated for their impact on the crystallinity, morphology, and surface properties of the synthesized α-alumina NP powders. Comprehensive analysis revealed that NH_4OH produced the smallest crystallite size (54.67 nm), the highest specific surface area (28.36 m² g⁻¹), and complete phase purity, as confirmed by XRD and Rietveld refinement. In contrast, the KOH-based synthesis resulted in larger crystallites, lower surface area, and minor secondary phase formation. Multiple crystallite size determination models

were applied to ensure accuracy and validate structural trends. UV-Vis spectroscopy indicated wide band gaps (5.4–5.5 eV) characteristic of α-alumina NPs, while DLS and zeta potential analyses confirmed the better colloidal stability of NH_4OH- and NaOH-derived samples compared to the KOH-derived sample. The dominant (113) growth orientation was preserved across all samples. TGA–DSC analysis further revealed that NH_4OH-derived samples exhibited higher residual mass, indicating superior thermal stability, while all samples exhibited α-Al_2O_3 formation occurring between 1047 and 1121 °C. TEM analysis of sample C (NH_4OH base) revealed uniformly distributed NPs with spherical morphology and minimal agglomeration. Particle size analysis confirmed the smallest average size (57.48 nm), consistent with XRD results. Samples A and B showed comparatively higher agglomeration and larger particle sizes. Overall, this work presents a detailed comparative approach to understanding how the base type governs the structural and functional attributes of α-alumina NPs. This study was limited to NaOH, KOH, and NH_4OH, but future work should explore other bases, scale up the NH_4OH-assisted route for industrial feasibility, and evaluate the synthesized α-alumina nanoparticles in applications like ceramics, catalysis, and photocatalysis.

Conflicts of interest

There are no conflicts to declare.

Data availability

Data will be available on request.

Acknowledgements

References

1 H. Li, Y. Li, J. Jiao and H. M. Hu, Alpha-alumina nanoparticles induce efficient autophagy-dependent cross-presentation and potent antitumour response, *Nat. Nanotechnol.*, 2011, **6**(10), 645–650, DOI: **10.1038/nnano.2011.153**.

2 Y. K. Park, E. H. Tadd, M. Zubris and R. Tannenbaum, Size-controlled synthesis of alumina nanoparticles from aluminum alkoxides, *Mater. Res. Bull.*, 2005, **40**(9), 1506–1512, DOI: **10.1016/j.materresbull.2005.04.031**.

3 A. Amirsalari and S. F. Shayesteh, Effects of pH and calcination temperature on structural and optical properties of alumina nanoparticles, *Superlattices Microstruct.*, 2015, **82**, 507–524, DOI: **10.1016/j.spmi.2015.01.044**.

4 P. Kathirvel, J. Chandrasekaran, D. Manoharan and S. Kumar, Preparation and characterization of alpha alumina nanoparticles by in-flight oxidation of flame synthesis, *J. Alloys Compd.*, 2014, **590**, 341–345, DOI: **10.1016/j.jallcom.2013.12.105**.

5 G. da Costa Cunha, L. P. C. Romão and Z. S. Macedo, Production of alpha-alumina nanoparticles using aquatic humic substances, *Powder Technol.*, 2014, **254**, 344–351, DOI: **10.1016/j.powtec.2014.01.008**.

6 S. S. Athari, Z. Pourpak, G. Folkerts, J. Garssen, M. Moin, I. M. Adcock and E. Mortaz, Conjugated Alpha-Alumina nanoparticle with vasoactive intestinal peptide as a Nano-drug in the treatment of allergic asthma in mice, *Eur. J. Pharmacol.*, 2016, **791**, 811–820, DOI: **10.1016/j.ejphar.2016.10.014**.

7 B. Ben-Nissan, A. H. Choi and R. Cordingley, Alumina ceramics, in *Bioceramics and their clinical applications*, Woodhead Publishing, 2008, pp. 223–242, DOI: **10.1533/9781845694227.2.223**.

8 P. Kaur, A. Khanna, N. Kaur, P. Nayar and B. Chen, Synthesis and structural characterization of alumina nanoparticles, *Phase Transitions*, 2020, **93**(6), 596–605, DOI: **10.1080/01411594.2020.1765245**.

9 A. H. Tavakoli, P. S. Maram, S. J. Widgeon, J. Rufner, K. Van Benthem, S. Ushakov and A. Navrotsky, Amorphous alumina nanoparticles: structure, surface energy, and thermodynamic phase stability, *J. Phys. Chem. C*, 2013, **117**(33), 17123–17130, DOI: **10.1021/jp405820g**.

10 S. N. S. Mohamad, N. Mahmed, D. S. C. Halin, K. A. Razak, M. N. Norizan and I. S. Mohamad, Synthesis of alumina nanoparticles by sol-gel method and their applications in the removal of copper ions (Cu^{2+}) from the solution, in *IOP Conference Series: Materials Science and Engineering*, IOP Publishing, 2019, vol. 701, No. 1, p. 012034, DOI: **10.1088/1757-899X/701/1/012034**.

11 S. Lamouri, M. Hamidouche, N. Bouaouadja, H. Belhouchet, V. Garnier, G. Fantozzi and J. F. Trelkat, Control of the γ-alumina to α-alumina phase transformation for an optimized alumina densification, *Bol. Soc. Esp. Ceram. Vidrio*, 2017, **56**(2), 47–54, DOI: **10.1016/j.bsecv.2016.10.001**.

12 F. Mirjalili, M. Hasmaliza and L. C. Abdullah, Size-controlled synthesis of nano α-alumina particles through the sol–gel method, *Ceram. Int.*, 2010, **36**(4), 1253–1257, DOI: **10.1016/j.ceramint.2010.01.009**.

13 W. L. Suchanek, Hydrothermal synthesis of alpha alumina (α-Al2O3) powders: study of the processing variables and growth mechanisms, *J. Am. Ceram. Soc.*, 2010, **93**(2), 399–412, DOI: **10.1111/j.1551-2916.2009.03399.x**.

14 K. Frikha, L. Limousy, J. Bouaziz, S. Bennici, K. Chaari and M. Jeguirim, Elaboration of alumina-based materials by solution combustion synthesis: A review, *C. R. Chim*, 2019, **22**(2–3), 206–219, DOI: **10.1016/j.crci.2018.10.004**.

15 M. A. Alam, S. Ahmed, D. Sarkar, R. K. Bishwas and S. A. Jahan, Preferred crystallographic design of monoclinic tenorite (CuO) nanocrystals by powder X-ray line diffraction, *Chem. Inorg. Mater.*, 2025, **7**, 100119, DOI: **10.1016/j.cinorg.2025.100119**.

16 P. K. Rao, P. Jana, M. I. Ahmad and P. K. Roy, Synthesis and characterization of zirconia toughened alumina ceramics prepared by co-precipitation method, *Ceram. Int.*, 2019, **45**(13), 16054–16061, DOI: **10.1016/j.ceramint.2019.05.121**.

17 A. Rajaeiyan and M. M. Bagheri-Mohagheghi, Comparison of sol-gel and co-precipitation methods on the structural properties and phase transformation of γ and α-Al2O3 nanoparticles, *Adv. Manuf.*, 2013, **1**(2), 176–182, DOI: **10.1007/s40436-013-0018-1**.

18 Z. Gholizadeh, M. Aliannezhadi, M. Ghominejad and F. S. Tehrani, High specific surface area γ-Al_2O_3 nanoparticles synthesized by facile and low-cost co-precipitation method, *Sci. Rep.*, 2023, **13**(1), 6131, DOI: **10.1038/s41598-023-33266-0**.

19 A. Jabbar, A. Abbas, N. Assad, M. Naeem-ul-Hassan, H. A. Alhazmi, A. Najmi and H. M. Amin, A highly selective Hg 2+ colorimetric sensor and antimicrobial agent based on green synthesized silver nanoparticles using Equisetum diffusum extract, *RSC Adv.*, 2023, **13**(41), 28666–28675.

20 A. B. Siddique, D. Amr, A. Abbas, L. Zohra, M. I. Irfan, A. Alhoshani and H. M. Amin, Synthesis of hydroxyethylcellulose phthalate-modified silver nanoparticles and their multifunctional applications as an efficient antibacterial, photocatalytic and mercury-selective sensing agent, *Int. J. Biol. Macromol.*, 2024, **256**, 128009.

21 N. Assad, M. Naeem-ul-Hassan, M. Ajaz Hussain, A. Abbas, M. Sher, G. Muhammad and M. Farid-ul-Haq, Diffused sunlight assisted green synthesis of silver nanoparticles using Cotoneaster nummularia polar extract for antimicrobial and wound healing applications, *Nat. Prod. Res.*, 2025, **39**(8), 2203–2217.

22 F. T. L. Muniz, M. R. Miranda, C. Morilla dos Santos and J. M. Sasaki, The Scherrer equation and the dynamical theory of X-ray diffraction, *Found. Crystallogr.*, 2016, **72**(3), 385–390.

23 S. Nasiri, M. Rabiei, A. Palevicius, G. Janusas, A. Vilkauskas, V. Nutalapati and A. Monshi, Modified Scherrer equation to calculate crystal size by XRD with high accuracy, examples Fe2O3, TiO2 and V2O5, *Nano Trends*, 2023, **3**, 100015.

24 P. Aguilar-Marín, L. Angelats-Silva, E. Noriega-Diaz, M. Chavez-Bacilio and R. Verde-Vera, Understanding the phenomenon of x-ray diffraction by crystals and related concepts, *Eur. J. Phys.*, 2020, **41**(4), 045501.

25 R. K. Bishwas, M. Alam and S. A. Jahan, Sustainable synthesis of nano-crystalline α-alumina from waste food packaging for efficient azithromycin removal, *J. Ind. Eng. Chem.*, 2025, DOI: 10.1016/j.jiec.2025.07.027.

26 M. A. Alam, R. K. Bishwas, S. Mostofa and S. A. Jahan, Crystallographic phase stability of nanocrystalline polymorphs TiO2 by tailoring hydrolysis pH, *S. Afr. J. Chem. Eng.*, 2024, **49**(1), 73–85.

27 R. K. Bishwas, M. A. Alam, D. Sarkar, S. Mostofa and S. A. Jahan, Crystallographic Phase Transformation of Nanocrystalline Ultrafine Alumina, *J. Indian Chem. Soc.*, 2025, 102119.

28 M. A. Alam, M. K. H. Shishir, D. Sarkar, R. K. Bishwas and S. A. Jahan, X-ray line diffraction study of preferred oriented hexagonal zincite nanocrystals: A crystallographic investigation, *J. Cryst. Grow.*, 2025, 128230, DOI: 10.1016/j.jcrysgro.2025.128230.

29 M. A. Alam, R. K. Bishwas, S. Mostofa and S. A. Jahan, Impact on preferred orientation and crystal strain behavior of nanocrystal anatase-TiO2 by X-ray diffraction technique, *S. Afr. J. Chem. Eng.*, 2024, **49**, 348–352, DOI: 10.1016/j.sajce.2024.07.002.

30 M. A. Alam, R. K. Bishwas, S. Mostofa, D. Sarkar and S. A. Jahan, X-ray crystallography derived diffraction properties of cuprite crystal as revealed by transmission electron microscopy, *Physics Open*, 2024, **20**, 100228.

31 X. Bao, J. Wang, X. Wu, C. He, H. Luo, Q. Bai and S. Zhao, The symmetry aspect of magnetocaloric effect in LaxBi0. 3-xCa0.7MnO3 manganites, *Phys. B*, 2023, **671**, 415410.

32 B. Herzog, A. Schultheiss and J. Giesinger, On the validity of Beer–Lambert law and its significance for sunscreens, *Photochem. Photobiol.*, 2018, **94**(2), 384–389.

33 Z. Khalid, A. Ali, A. B. Siddique, Y. Zaman, M. F. Sibtain, A. Abbas and M. S. Alwethaynani, Causonis trifolia-based green synthesis of multifunctional silver nanoparticles for dual sensing of mercury and ferric ions, photocatalysis, and biomedical applications, *RSC Adv.*, 2025, **15**(21), 16879–16893.

34 C. Giannini, M. Ladisa, D. Altamura, D. Siliqi, T. Sibillano and L. De Caro, X-ray diffraction: a powerful technique for the multiple-length-scale structural analysis of nanomaterials, *Crystals*, 2016, **6**(8), 87.

35 R. K. Bishwas, M. A. Alam and S. A. Jahan, Crystallographic and morphological characterization of high-crystalline α-alumina nanoparticles: A comprehensive X-ray diffraction and transmission electron microscopy study, *Chem. Phys. Lett.*, 2025, 142245.

36 M. A. Alam, S. I. Sadia, M. K. H. Shishir, R. K. Bishwas, S. Ahmed, S. M. Al-Reza and S. A. Jahan, Crystallinity

37 integration and crystal growth behavior study of preferred oriented (111) cubic silver nanocrystal, *Inorg. Chem. Commun.*, 2025, **173**, 113834, DOI: 10.1016/j.inoche.2024.113834.

37 S. Ahmed, M. A. Alam, S. I. Sadia, R. K. Bishwas, M. Hasanuzzaman and S. A. Jahan, Stoichiometry low-temperature dynamics crystal growth interpret of zinc oxide hexagonal nanocrystals, *Next Mater.*, 2025, **7**, 100636.

38 M. A. Alam, S. Ahmed, R. K. Bishwas, D. Sarkar and S. A. Jahan, Crystal growth behavior interpret of co-precipitated derived nickel oxide (NiO) nanocrystals, *Nano-Struct. Nano-Objects*, 2025, **42**, 101494, DOI: 10.1016/j.nanoso.2025.101494.

39 J. I. Langford, D. Louër and P. Scardi, Effect of a crystallite size distribution on X-ray diffraction line profiles and whole-powder-pattern fitting, *Appl. Crystallogr.*, 2000, **33**(3), 964–974.

40 M. A. Alam, S. Ahmed, R. K. Bishwas, S. Mostofa and S. A. Jahan, X-ray crystallographic diffraction study by whole powder pattern fitting (WPPF) method: Refinement of crystalline nanostructure polymorphs TiO2, *S. Afr. J. Chem. Eng.*, 2025, **51**, 68–77, DOI: 10.1016/j.rinma.2025.100673.

41 A. S. Jbara, Z. Othaman, H. A. Aliabad and M. A. Saeed, Electronic and Optical Properties of γ-and-Alumina by First Principle Calculations, *Adv. Sci., Eng. Med.*, 2017, **9**(4), 287–293.

42 R. C. R. Santos, E. Longhinotti, V. N. Freire, R. B. Reimberg and E. W. S. Caetano, Elucidating the high-k insulator α-Al2O3 direct/indirect energy band gap type through density functional theory computations, *Chem. Phys. Lett.*, 2015, **637**, 172–176.

43 S. Ciraci and I. P. Batra, Electronic structure of α-alumina and its defect states, *Phys. Rev. B:Condens. Matter Mater. Phys.*, 1983, **28**(2), 982, DOI: 10.1103/PhysRevB.28.982.

44 R. Shah, D. Eldridge, E. Palombo and I. Harding, Optimisation and stability assessment of solid lipid nanoparticles using particle size and zeta potential, *J. Phys. Sci.*, 2014, **25**, 1.

45 M. Kanwal, M. Sher, A. Abbas, S. Akhtar, A. B. Siddique, M. N. Ul Hasan and H. M. Amin, Dual colorimetric sensing of Hg(II) and Fe(III) using sulfanilamide-stabilized silver nanoparticles and evaluating their photodegradation and antibacterial properties, *J. Water Process Eng.*, 2025, **75**, 107981.

46 S. Ullah, R. Khalid, M. F. Rehman, M. I. Irfan, A. Abbas, A. Alhoshani and H. M. Amin, Biosynthesis of phyto-functionalized silver nanoparticles using olive fruit extract and evaluation of their antibacterial and antioxidant properties, *Front. Chem.*, 2023, **11**, 1202252.

47 S. Amin, M. Sher, A. Ali, M. F. Rehman, A. Hayat, M. Ikram and H. M. Amin, Sulfonamide-functionalized silver nanoparticles as an analytical nanoprobe for selective Ni(II) sensing with synergistic antimicrobial activity, *Environ. Nanotechnol., Monit. Manage.*, 2022, **18**, 100735.

48 D. Sun, S. Kang, C. Liu, Q. Lu, L. Cui and B. Hu, Effect of zeta potential and particle size on the stability of SiO2

nanospheres as carrier for ultrasound imaging contrast agents, *Int. J. Electrochem. Sci.*, 2016, **11**(10), 8520–8529.

49 H. Arami, M. Mazloumi, R. Khalifehzadeh and S. K. Sadrnezhaad, Bundles of self-assembled boehmite nano-strips from a surfactant free hydrothermal route, *J. Alloys Compd.*, 2008, **461**(1–2), 551–554.

50 F. Mirjalili, L. C. Abdullah, H. Mohamad, A. Fakhru′ l-Razi, A. B. Dayang Radiah and R. Aghababazadeh, Process for Producing Nano-Alpha-Alumina Powder, *Int. Scholarly Res. Not.*, 2011, **2011**(1), 692594.

51 M. Y. Manuputty, C. S. Lindberg, M. L. Botero, J. Akroyd and M. Kraft, Detailed characterisation of TiO2 nano-aggregate morphology using TEM image analysis, *J. Aerosol Sci.*, 2019, **133**, 96–112.

52 M. Ates, V. Demir, Z. Arslan, J. Daniels, I. O. Farah and C. Bogatu, Evaluation of alpha and gamma aluminum oxide nanoparticle accumulation, toxicity, and depuration in Artemia salina larvae, *Environ. Toxicol.*, 2015, **30**(1), 109–118.

53 A. B. Siddique, M. A. Shaheen, A. Abbas, Y. Zaman, H. M. Amin, M. M. Alam and A. Ali, Sunlight-assisted greenly synthesised silver nanoparticles for highly selective mercury ion sensing, biomedical and photocatalytic applications, *Int. J. Environ. Anal. Chem.*, 2025, 1–23.